In the format provided by the authors and unedited.

Optically controlling the emission chirality of microlasers

N. Carlon Zambon [1,4]*, **P. St-Jean** [1,4]*, **M. Milićević**[1], **A. Lemaître** [1], **A. Harouri**[1], **L. Le Gratiet**[1], **O. Bleu**[2], **D. D. Solnyshkov** [2], **G. Malpuech**[2], **I. Sagnes**[1], **S. Ravets**[1], **A. Amo** [3] and **J. Bloch**[1]

[1]Centre de Nanosciences et de Nanotechnologies (C2N), CNRS - Université Paris-Sud - Université Paris-Saclay, Palaiseau, France. [2]Institut Pascal, PHOTON-N2, Université Clermont Auvergne, CNRS, SIGMA Clermont, Clermont-Ferrand, France. [3]Univ. Lille, CNRS, UMR 8523 – PhLAM – Physique des Lasers Atomes et Molécules, Lille, France. [4]These authors contributed equally: N. Carlon Zambon, P. St-Jean. *e-mail: nicola.carlon-zambon@c2n.upsaclay.fr; philippe.st-jean@c2n.upsaclay.fr

Optically controlling the chirality of microlasers:
Supplemental materials

N. Carlon Zambon,[1, *] P. St-Jean,[1, *] M. Milićević,[1] A. Lemaître,[1] A. Harouri,[1] L. Le Gratiet,[1]
I. Sagnes,[1] O. Bleu,[2] D. D. Solnyshkov,[2] G. Malpuech,[2] S. Ravets,[1] A. Amo,[3] and J. Bloch[1]

[1]*Centre de Nanosciences et de Nanotechnologies (C2N),*
CNRS - Université Paris-Sud / Paris-Saclay, Marcoussis, France
[2]*Institut Pascal, PHOTON-N2, CNRS - University Clermont Auvergne, Clermont-Ferrand, France.*
[3]*Physique des Lasers, Atomes et Molécules (PhLAM), CNRS - Université de Lille, Lille, France*

I. SAMPLE DESCRIPTION

The benzene microstructures were fabricated from a planar semiconductor heterostructure grown by molecular beam epitaxy, consisting of a λ Fabry-Pérot cavity embedding a 17 nm wide $In_{0.04}Ga_{0.96}As$ quantum well. The cavity is formed by a GaAs spacer enclosed between two $Al_{0.10}Ga_{0.90}As / Al_{0.95}Ga_{0.05}As$ distributed Bragg reflectors (DBR), with 32 and 36 pairs of layers at the top and bottom, respectively. The cavity spacer presents a thickness gradient, allowing to tune the cavity mode with respect to the gain spectral dependence. The measured quality factor of the planar cavity is $Q \approx 4 \cdot 10^4$, limited mainly by residual absorption in the spacer. The cavity was grown on a double-side polished 350 μm thick GaAs substrate, in order to allow operation in transmission geometry. The planar structure was then dry-etched to form coupled micropillars structures with different pillar diameters and inter-pillar distances. Finally, to prevent multiple reflections at the interface between GaAs and vacuum we deposited an anti-reflection coating (ARC), consisting of a silicon oxynitride quarter wavelength layer. An overall view of the planar structure is sketched in Fig. 1 A.
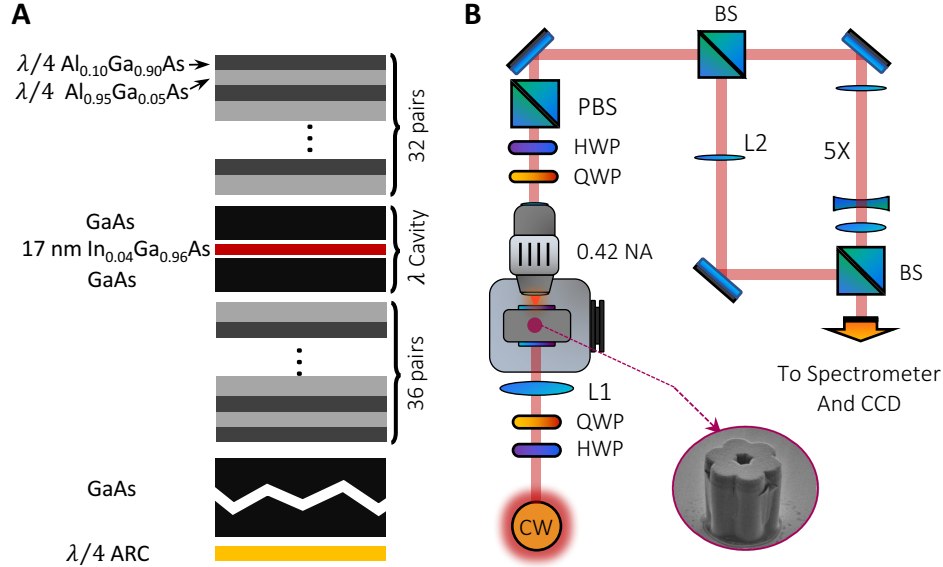

FIG. 1. **Sample and setup details**: (A) Cross-section of the semiconductor heterostructure forming the laser cavity. (B) Sketch of the experimental setup. The inset shows a scanning electron microscopy image of a device.

II. SETUP AND MEASUREMENTS

A sketch of the experimental setup used in this work is presented in Fig. 1 B. The sample was held in a closed-cycle cryostat where the temperature could be actively stabilized between 4K and room temperature. The device was pumped on the epitaxial side (top in Fig. 1 A) with a continuous wave Ti:Sapphire laser focused by a lens with

a focal length of 100 mm producing a 20 μm FWHM gaussian spot, ensuring a quasi-uniform illumination of the structure. The incident polarization state of the pump was controlled with a $\lambda/4$ waveplate, and its wavelength was set to 770 nm corresponding to one of the reflectivity minima of the DBRs.

The emission from the microstructure was collected from the substrate (bottom in Fig. 1 A) side using a 0.42 NA objective and its polarization state was analyzed with a polarizing beam splitter (PBS) together with a quarter-wave plate (QWP) and a half-wave plate (HWP) allowing to realize a full polarization tomography. Energy resolved measurements (e.g. in Fig. 1 B, 2 D-F, 3 D-F and 4 D of the main text), were realized with a CCD camera coupled to a spectrometer; for measurements without spectral resolution (e.g. Fig. 2 C,G-J, 3 C,G-J and 4 C,E,F of the main text), we used the same setup but analyzed the detection at the 0th order of the spectrometer.

For the measurements that were realized without circular polarization filtering, we used only a polarizing beam splitter (PBS) in the detection path to select a well-defined linear polarization component of the emission. This was done in order to get rid of the effects of the polarization-dependent reflectivity of the spectrometer grating by sending always the same linear polarization in it. It is important to point out that this selection of a single linear polarization in the detection path does not affect the emission pattern of the modes that are circularly-polarized (i.e. $\psi_{2,3}$ which are the important modes for realizing our OAM lasing scheme), whereas it results in the formation of dark regions for modes which have a linearly-polarized emission pattern (i.e. $\psi_{1,4}$ which are radially and azymuthally polarized). This can be seen in Fig. 2 where we present real space images of the beam for circularly and linearly polarized excitation for a molecule with inter-pillar distance of 2.4 μm (where lasing occurs in the $|\ell| = 2$ manifold). The linearly polarized excitation triggers lasing in ψ_4, presenting a linear polarization; the circularly polarized one (σ_+ in this case) triggers lasing in ψ_3 which is unaffected by the linear polarization detection (H corresponds to the linear polarization selected by the PBS for all measurements without circular polarization selection).
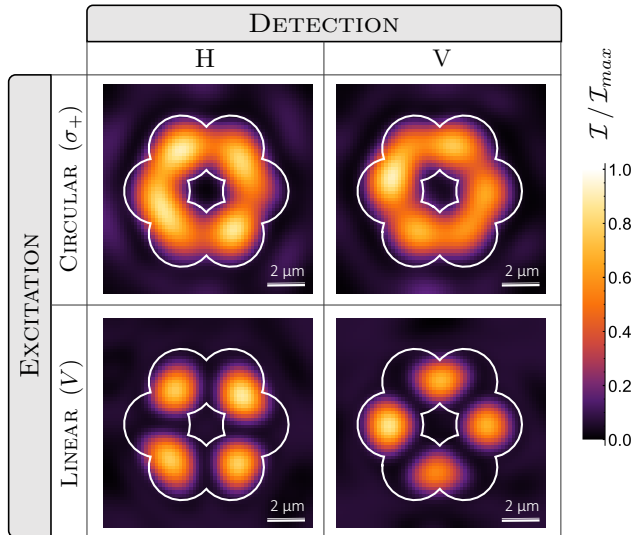

FIG. 2. **Emission under linearly and circularly polarized excitation.** Real space images of the emission (without spectral filtering) for circularly polarized (A-B) and linearly polarized (C-D) excitations. All images are taken under a linear polarization: horizontal for (A) and (C) and vertical for (B) and (D).

To realize the interferometry measurements, the optical path was separated in a modified Mach-Zender interferometer: in one arm (signal), a lens with a 750 mm focal length imaged the real space emission on the spectrometer entrance, and, in the second arm (reference), an expanded image of the emission was created using a 5× magnifying telescope. When recombining the two images, we can overlap the emission of the whole microstructure with a magnified image of one of the pillars. It was possible to consider the magnified beam as a phase reference, because the phase gradient within the area of a single pillar is much smaller than π. Therefore, by slightly tilting the direction of the reference beam with respect to that of the signal beam after their recombination, we could produce fringe patterns as shown in the main text (e.g. in Fig. 2,3 G,I and 4 E,F).

III. RETRIEVING THE PHASE MAPS

In the main text we present in Fig. 2 and 3 interferograms for the $\ell = \pm 1$ and $\ell = \pm 2$ modes and, next to them, the corresponding phase maps. In order to extract these maps we used an off-diagonal Fourier filtering technique which we schematically depict in Fig. 3. The idea is that if the signal and reference beams are described by the complex amplitudes:

$$
\begin{aligned}
\mathcal{A}_s &= A_s(\mathbf{r})e^{-i(\omega t - \mathbf{k}_s \cdot \mathbf{r} + \phi)} \\
\mathcal{A}_r &= A_r(\mathbf{r})e^{-i(\omega t - \mathbf{k}_r \cdot \mathbf{r})},
\end{aligned}
\tag{1}
$$

then the fringe intensity pattern produced at the spectrometer entrance plane ($z = 0$) will be given by:

$$
\begin{aligned}
I(\mathbf{r}) &= |\mathcal{A}_s + \mathcal{A}_r|^2 \\
&= |A_s|^2 + |A_r|^2 + \left(A_s A_r^* e^{-i(\Delta \mathbf{k} \cdot \mathbf{r} + \phi)} + c.c. \right),
\end{aligned}
\tag{2}
$$

where $\Delta \mathbf{k}$ is the in-plane wavevector difference between the signal and reference beams. One example of these fringe patterns is provided in Fig. 3 A. If we Fourier-transform the fringe pattern $\tilde{I}(\mathbf{k}) = \tilde{\mathcal{F}}[I]$, the first two terms in equation (2) produce a peak centered at the reciprocal space origin, whereas the third and fourth term correspond to two satellite peaks translated by $\pm \Delta \mathbf{k}$ with respect to the origin. In Fig. 3 B we show the modulus of the Fourier-transformed fringe pattern. These satellite peaks carry the information on the wavefront phase, which can be retrieved by operating a rigid translation of the reciprocal space by $\pm \Delta \mathbf{k}$ and filtering-out all the other peaks (see Fig. 3 C). The remaining peak corresponds to $\tilde{\mathcal{F}}[A_s A_r^* e^{-i\phi}]$. Then, by inverse Fourier transforming this complex amplitude and taking its argument, we can extract the phase pattern (Fig. 3 D) associated to the initial fringe pattern (Fig. 3-A). Remarkably, a clear signature of the phase singularity present in the fringe pattern, can be directly observed also in reciprocal space, where it manifests as a dark spot in the middle of the side-peaks.
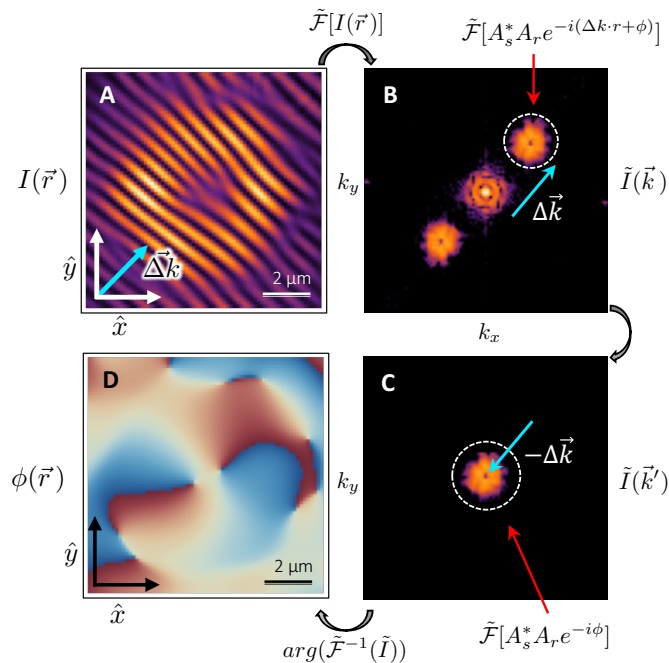

FIG. 3. **Retrieving the wavefront phase**: (A)-Typical inteferrence pattern for the $|-2, \sigma_+\rangle$ mode (from Fig.3-G in the main text), produced by interfering the emission and reference arm with an in-plane wavevector difference $\Delta \mathbf{k}$. (B) Absolute value of the digitized interferogram fast Fourier transform (FFT). (C) After a rigid translation of the FFT by $-\Delta \mathbf{k}$ we apply a radial low-pass filter. (D) Real space image of the emission phase $\phi(r)$, obtained as the argument of the inverse FFT.
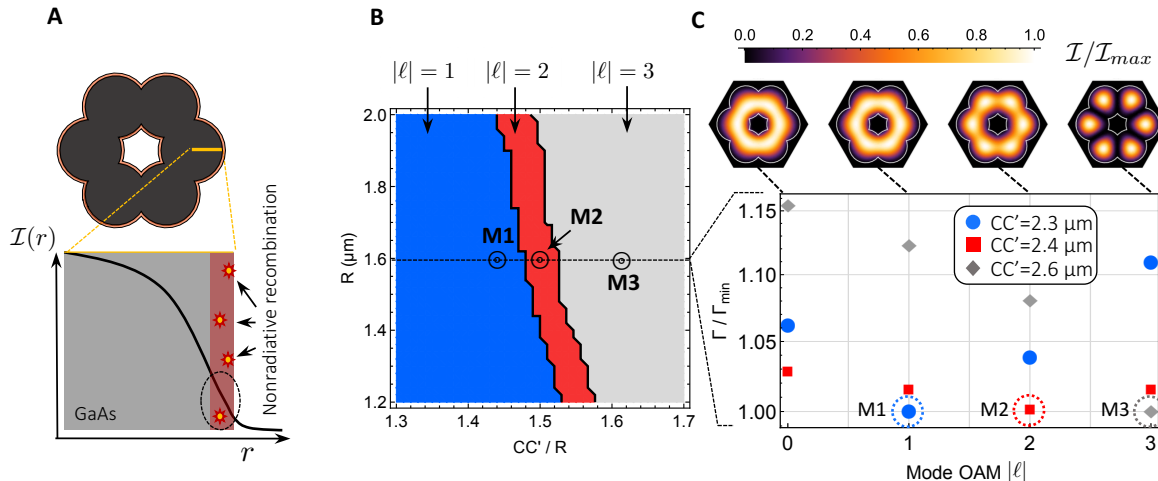
FIG. 4. **Lasing mode selection**: (A) Schematic representation of the device; the orange region along the perimeter highlights the region where the density of nonradiative recombination centers is the highest. The zoom-in shows an image of the lateral section of one pillar near the outer edge, and the solid line represents a typical radial profile of a mode. (B) Mapping presenting which manifold is expected to exhibit the lowest non-radiative losses as a function of the inter-pillar distance and pillar radius. The blue, red and gray areas correspond to regions where, respectively, $|\ell = 1, 2, 3|$ manifold exhibits the lowest losses. The black circles correspond to the three different devices (M1, M2 and M3) investigated in this work. (C) Plot of the calculated non-radiative losses associated to each scalar eigenmode, where Γ_{min} corresponds to the lowest value calculated. Blue circles, red squares and grey diamonds correspond to structures with pillar radius of R = 1.6 μm and an inter-pillar distance of, respectively, $CC' = (2.3, 2.4, 2.6)\mu$m. On top we show the calculated scalar eigenmodes intensity profile for $CC' = 2.4\mu$m.

IV. SELECTION OF THE LASING MODE

In the main text, we show that two microstructures, labeled M1 and M2, having the same radius (1.6 μm) but different interpillar distance, lase in modes $|\ell| = 1$ and $|\ell| = 2$ respectively. In this section we provide an explanation based on a simple model with a minimal number of parameters describing how it is possible to tune the relative gain/loss ratio of each OAM manifold (and thus select in which of them lasing occurs) by changing this interpillar distance.

In this model, we consider the gain of each mode to be identical, because any spectral or spatial dependences of the gain can be neglected; the reasons for this are the following. Firstly, the scalar eigenmodes of the photonic molecule (i.e. $|\ell| = 0, ..., 3$) span over only few meV, a small energy scale compared to the typical spectral width of the gain profile. This allows neglecting any significant spectral dependence of the gain. Secondly, since the structure was evenly illuminated, we can as well consider that the spatial overlap between the gain medium and every mode is nearly identical.

In our model, the selection of the lasing manifold is therefore solely determined by the relative losses associated to each manifold. In our micro-cavities, losses associated to photons leaking through the mirrors (i.e. the radiative lifetime) are identical for each mode. However, the dry etching process creates near the pillar edges a high density of nonradiative recombination centers (NRC): these NRC represent the main contribution to the variation of losses from one mode to the other, because the different modes do not overlap similarly with the edge of the structure.

We can deduce the relative contribution of these nonradiative losses by computing the overlap integral of each eigenmode with the NRC density profile. For simplicity, we assume the latter to be uniform over a thickness δR along the edges of the structure, as sketched in Fig. 4 A. The scalar photonic eigenmodes of the microstructure were obtained by finite element methods: the hexagonal molecules were described as six overlapping infinite waveguides with the same transverse profile as the microstructure, and we solved the associated Helmholtz equation. The refractive index of the waveguides was chosen to match the effective refractive index of the vertical cavity ($n_{\text{eff}} \approx 3.46$ at 10 K). This effective refractive index can be computed by weighting the refractive index profile $n(z)$ by the vertical field profile $u(z)$ obtained for a planar cavity with transfer matrix methods.

According to these calculations, we show in Fig. 4 B which mode has the lowest nonradiative contribution (and therefore should lase) as a function of the micropillar radius R and inter-pillar distance CC' (red, blue and gray areas correspond to $|\ell| = 1$, $|\ell| = 2$ and $\ell = 3$ manifolds, respectively). We see that for sufficiently small inter-pillar

distance the favoured manifold is $|\ell| = 1$ whereas for large CC' values the favoured mode is $\ell = 3$; in-between these two regions, when $CC' \sim 3/2\,R$, the $|\ell| = 2$ mode is favoured. This behaviour stems from the competition between two different mechanisms. On the one hand, modes with increasing $|\ell|$ have a profile that peaks at larger values of the radial coordinate, thus having a greater overlap with the outer edge of the microstructure. On the other hand, modes with a smaller $|\ell|$ present a larger overlap with inter-pillar regions where the density of NRC is the largest; this second effect is more pronounced as CC' increases.

The exact range of inter-pillar distances CC'/R, as a function of R, where the $|\ell| = 2$ mode is favoured, depends on the thickness of the nonradiative recombination region considered. In order to match the experimental observations (black circles), we had to set $\delta R \approx 0.1\,\mu$m, which is a reasonable value for the etching technique used. The black circles correspond to the microlaser structures presented in Fig. 2 and 3 in the main manuscript (labeled as M1 and M2) and to a structure with $CC' = 2.6\,\mu$m (M3) where lasing occurs in the $\ell = 3$ manifold (see Section V). In Fig. 4 C, we plot the relative nonradiative linewidth Γ/Γ_{min}, where $\Gamma = \hbar/\tau_{NR}$ and Γ_{min} corresponds to the lowest value calculated for Γ. On top of this panel, we present the typical intensity profile of each scalar eigenmode of the system, for microstructures associated to the black circles in Panel B (indicating the structures M1,M2 and M3).

Finally, we have neglected more complex nonlinear contributions to the balance of population dynamics such as gain saturation, spectral and spatial hole burning or band gap renormalization. This was possible, because our minimalist model, which relates the losses to the overlap of the modes with the outer contour of the molecule, was sufficient to properly reproduce, for all excitation powers, the dependence of the lasing manifold on the device shape without these contributions.
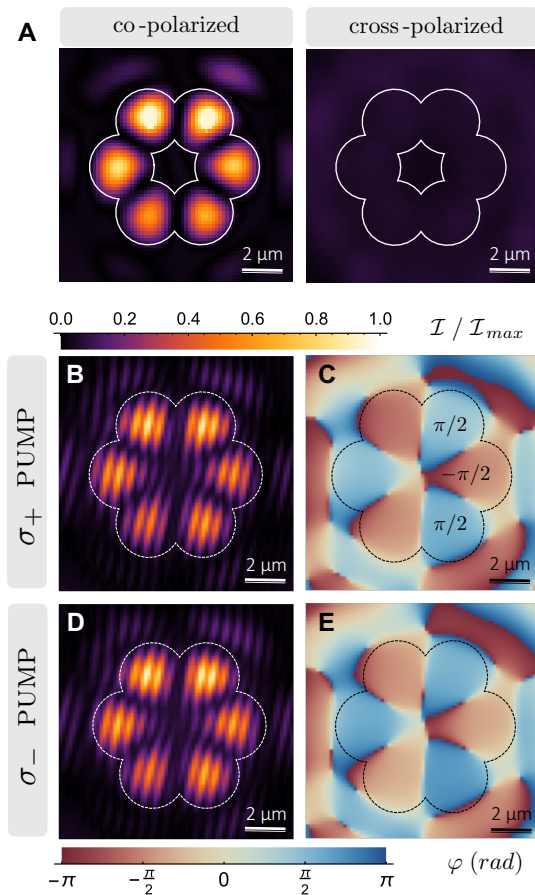

FIG. 5. **Lasing in the $|\ell| = 3$ manifold**: (A) Co- and cross-polarized real space images of the emission under σ_+ polarized pump. The inter-pillar distance here is $CC' = 2.6\,\mu$m, the images were taken for an incident excitation density of $\approx 0.7\,\text{kW}/cm^2$. (B,D) Interference pattern obtained as described above for a σ_+ and σ_- polarized pump, respectively. (C,E) Corresponding phase maps showing the characteristic π phase jumps between neighbouring pillars.

V. LASING IN $\ell=3$ MODES

In figure 5 A, we present real space images of the emission (at a pumping power well above the lasing threshold) for a molecule (labeled M3) with inter-pillar distance $CC' = 2.6\mu$m; in this molecule, lasing occurs in the $\ell = 3$ states. We see that for a σ_+-polarized pump, the emission is strongly σ_+-polarized and presents six bright lobes localized at the center of each pillar with vanishing intensiy in-between. Interference patterns under σ_+ and σ_- excitations are presented respectively in Fig. 5 B and D; the associated phase maps are reported in Fig. 5 C and E. The π phase jump between adjacent pillars demonstrate that in molecule M3 lasing is triggered in the $\ell = 3$ mode. As mentioned in the main text, this mode does not exhibit a net chirality, as it presents a mirror symmetry.

VI. EXTENDED CHARACTERIZATION OF THE LASING EMISSION

In this section, we present an extended characterization of the properties of the emission from both M1 ($|\ell| = 1$) and M2 ($|\ell| = 2$) microlasers.

Firstly, Fig. 6 B (M1) and 6 C (M2) show the evolution of the emission spectrum as a function of pump power, for each data point of the IP curves shown in Fig 2B and Fig 3B of the main text. In the power range explored, we can observe that above the lasing threshold all the emission sidebands are suppressed (~ 20 dB for M1 and ~ 30 dB for M2) and that no mode switching is observed.

Secondly, Fig. 6 B and D present the evolution of the emission linewidth as a function of the excitation power for the M1 ($|\ell| = 1$) and M2 ($|\ell| = 2$) microlasers, respectively. Upon increasing the pump power, we observe an initial broadening of the peak, associated to the transition from the strong to the weak coupling regime of the microcavity. Then, the linewidth rapidly decreases as it approaches the lasing threshold. Finally, above threshold, the linewidth is only limited by the spectrometer resolution ($\sim 40~\mu eV$).
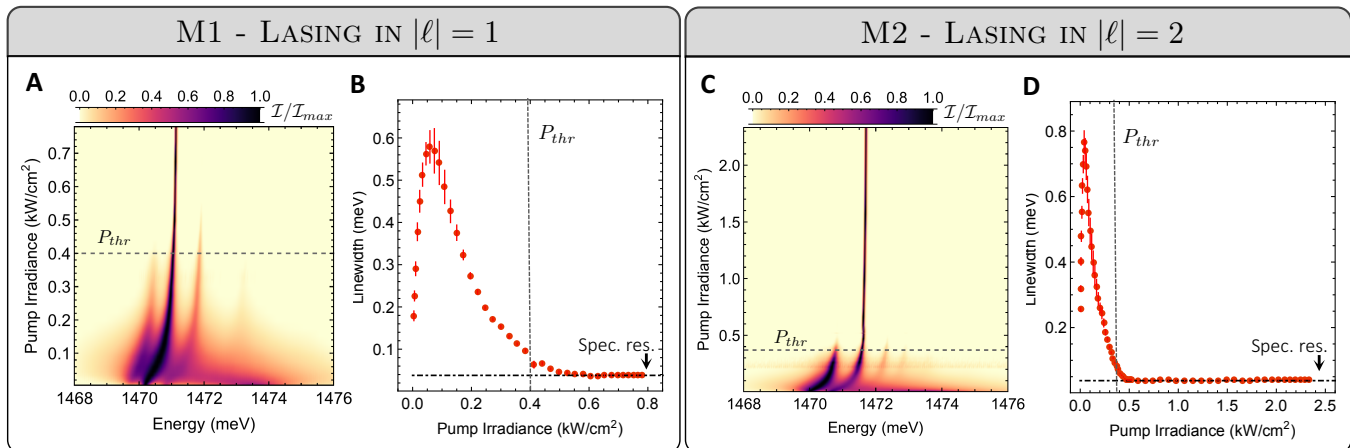

FIG. 6. **Lasing properties for M1 and M2 microlasers.** (A) and (C) Emission spectra as a function of the excitation power for microlasers M1 (A) and M2 (C). (B) and (d) Evolution of the emission linewidth as a function of the excitation power for microlasers M1 (B) and M2 (D). The dashed line indicates the spectrometer resolution ($\sim 30~\mu eV$).

VII. FINE STRUCTURE IN N-PILLAR RING MOLECULES

The discrete rotational symmetry of benzene photonic molecules allows defining a quantum number $\ell = 0, \pm 1, \pm 2, 3$ associated to the orbital angular momentum of eigenmodes which is related to their relative phase between the pillars. As described in the main text, the spin-orbit coupling of photons in these molecules, arising from the polarization-dependent hopping, splits the $\ell = \pm 1$ and $\ell = \pm 2$ manifolds to form 3-levels fine structures (see Fig. 1 (c) and (d) of the main text) that are necessary to implement our lasing scheme. Importantly, such a fine structure does not only appear in benzene molecules, but in any n-pillars ring molecules, with n even and > 4, allowing to extend the scheme to generate arbitrarily large OAM using molecules with a larger number of pillars.

The point of this section is (1) to show how the emergence of this interesting fine structure can be understood in benzene molecules by considering the symmetry of the Hamiltonian, and (2) to extend this argument to molecules with arbitrary n. We demonstrate that they present the necessary 3-level fine structures in the $|\ell| = 1$ and $|\ell| = n/2 - 1$ manifolds.

A. Fine structure in benzene molecules

The group of all symmetry operations of a benzene photonic molecule is C_{6v}. Contrary to real benzene molecules that present D_6 symmetry, our devices do not exhibit an out-of-plane mirror symmetry; this two groups are however isomorphic and lead to identical conclusions. The character table of C_{6v} is presented in Table I, where A_i and B_i are unidimensional irreducible representations (irreps) of the group. E_i are two-dimensional irreps; E (identity), C_n ($2\pi/n$ rotations) and σ_v (σ_d) (reflections across vertical planes that cross two opposite pillars (links)) are the symmetry operations of the group.

Modes	Functions	C_{6v}	E	C_6	C_3	C_2	σ_v	σ_d
$\ell = 0$	z	A_1	1	1	1	1	1	1
		A_2	1	1	1	1	-1	-1
$\ell = 3$		B_1	1	-1	1	-1	1	-1
		B_2	1	-1	1	-1	-1	1
$|\ell| = 1$	(x, y)	E_1	2	-2	-1	1	0	0
$|\ell| = 2$		E_2	2	2	-1	-1	0	0
		$\Gamma^{(\text{scalar})}$	6	0	0	0	2	0

TABLE I. Character table of the point group C_{6v}. The last line presents the characters of the reducible representation associated to scalar wave-functions of the benzene photonic molecule. The first and second columns respectively present scalar modes of the benzene and coordinates that transform according to the corresponding irreps presented in the third column.

One possible basis for the scalar wave-functions of the molecule (i.e. the eigenmodes without considering the spin) is given by the ground state of each pillar (ψ_{1-6}); the eigenmodes of the systems can thus be expressed in the form of a vector $\Psi = (\psi_1, \psi_2, \psi_3, \psi_4, \psi_5, \psi_6)^\dagger$. One can then identify a set of matrices that describe how this vector transforms under each symmetry operation of the group.

Since the Hamiltonian of the system commutes with every symmetry operator, this set of matrices forms a reducible representation of the group (that we label $\Gamma^{(\text{scalar})}$). The trace (character) of each of these matrices is given in the bottom line of Table I, allowing to deduce the following decomposition in irreps:

$$\Gamma^{(\text{scalar})} = A_1 \oplus B_1 \oplus E_1 \oplus E_2. \tag{3}$$

This decomposition indicates that the eigenspectrum of the scalar system is formed of 4 energy levels: 2 non-degenerate states transforming according to A_1 and B_1 and 2 degenerate doublets transforming as E_1 and E_2.

Inspection of the character table shows that the eigenmodes transforming according to A_1 and B_1 are, respectively, symmetric under all symmetry operations of the group (i.e. $\ell = 0$) and anti-symmetric under $2\pi/6$ rotations (i.e. $\ell = 3$). Furthermore, the doublets transforming as E_1 and E_2 correspond, respectively, to the $|\ell| = 1$ and $|\ell| = 2$ manifold (the value of the angular momentum is extracted directly from the wave-function of each mode, which are determined by expanding generators associated to each irreps, see Ref. [1]). Although group theory does not provide information on the relative energy of these different states, it is possible to spectrally order them, because their energy scales with the phase gradient associated to the angular momentum ($A_1 - E_1 - E_2 - B_1$), as presented in the left part of Fig. 7.

In order to take into account the spin of photons, one needs to identify the irreps that transform identically as this spin moment: for the C_{nv} symmetry groups, $\ell = \pm 1$ angular momenta transform as E_1. Then, to retrieve the energy levels of our benzene molecule in the presence of spin-orbit coupling, we consider the tensor product between the E_1 and the scalar representation:

$$\Gamma^{(\mathrm{spin})} \otimes \Gamma^{(\mathrm{scalar})} = E_1 \otimes (A_1 \oplus B_1 \oplus E_1 \oplus E_2)$$
$$= \underbrace{E_1}_{\ell=0} \oplus \underbrace{E_2}_{\ell=3} \oplus \underbrace{A_1 \oplus A_2 \oplus E_2}_{|\ell|=1} \oplus \underbrace{B_1 \oplus B_2 \oplus E_1}_{|\ell|=2}. \tag{4}$$

This decomposition shows the effect of spin-orbit coupling on the fine structure, which is summarized in Fig. 7. In the spin-coupled basis, the $\ell = 0$ and $\ell = 3$ states become two-fold degenerate, due to the spin degeneracy, and transform respectively as E_1 and E_2 irreps. More importantly, the $\ell = 1$ ($\ell = 2$) manifolds split to form a 3-level fine structure formed from two non-degenerate states transforming as A_1 and A_2 for $|\ell| = 1$ (B_1 and B_2 for $|\ell| = 2$), and a doublet transforming as E_1 (E_2).
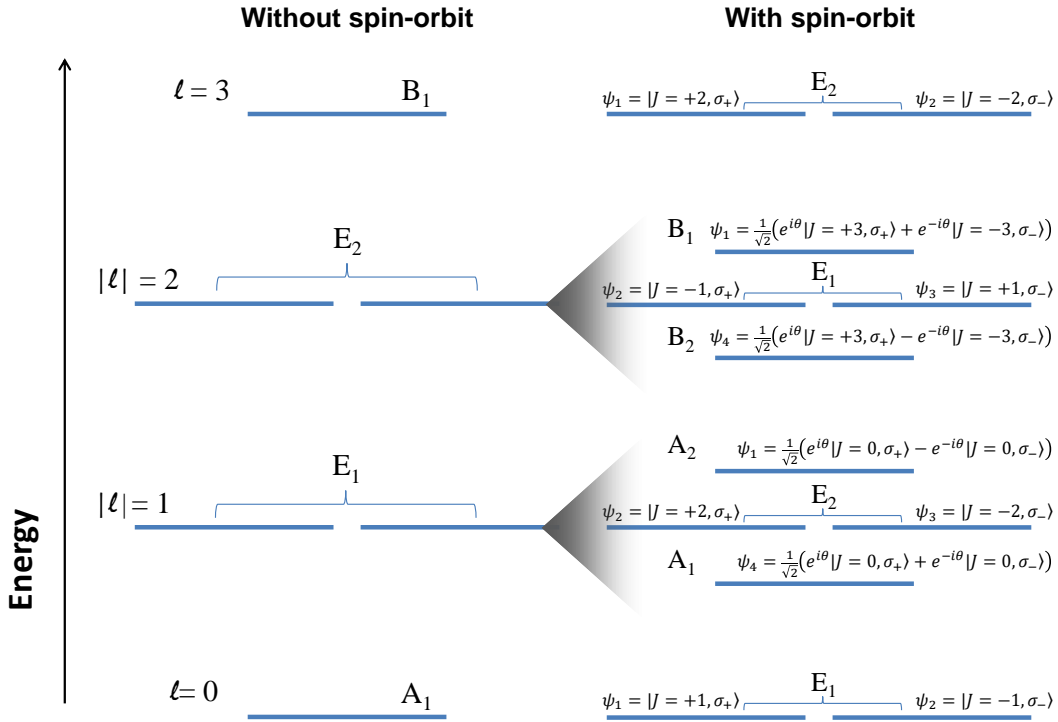

FIG. 7. Energy levels fine structure of a benzene photonic molecule without (left) and with (right) spin-orbit coupling. The irreps and wave-function (in the basis $|J, S\rangle$) of each state is presented. Here, the phase $\theta = 2\pi/6$.

By inspection of the symmetry of every eigenstate of the fine structure, it is possible to retrieve explicitly the wave-functions of each of these states. For the $\ell = 1$ manifold, states that transform as $A_{1,2}$ are symmetric under $2\pi/6$ rotations, indicating that they carry a total angular momentum $\vec{J} = \vec{L} + \vec{S} = 0$ (when considering spin-orbit coupling, ℓ and S are no longer good quantum numbers, but J is); furthermore, A_1 (A_2) is symmetric (anti-symmetric) under reflections $\sigma_{v,d}$. Therefore, the associated wave-functions (in the $|J, S\rangle$ basis) are:

$$\psi(A_1) = \frac{1}{\sqrt{2}}[e^{i\theta} |J = 0, \sigma_+(\ell = -1)\rangle + e^{-i\theta} |J = 0, \sigma_-(\ell = +1)\rangle]$$
$$\psi(A_2) = \frac{1}{\sqrt{2}}[e^{i\theta} |J = 0, \sigma_+(\ell = -1)\rangle - e^{-i\theta} |J = 0, \sigma_-(\ell = +1)\rangle]. \tag{5}$$

in these equations, we have indicated the value of ℓ in each ket. Here, the phase $\theta = 2\pi/6$ accounts for the 6-fold rotational symmetry of the wave-function.

Wave-functions associated to the E_2 doublet form conjugated partners with a total angular momentum $J = 2$, but opposite chiralities (E_2 is associated to modes presenting two quanta of angular momentum, see character table):

$$\psi_\pm(E_2) = |J = \pm 2, \sigma_\pm(\ell = \pm 1)\rangle. \tag{6}$$

In the $|\ell| = 2$ manifold, states that transform according to $B_{1,2}$ are anti-symmetric under $2\pi/6$ rotations, indicating modes with total angular momentum $J = 3$; furthermore, B_1 is symmetric (anti-symmetric) under σ_v (σ_d) reflections (and vice-versa for B_2). Therefore, the associated wave-functions are:

$$\psi(B_1) = \frac{1}{\sqrt{2}}[e^{i\theta}|J = 3, \sigma_+(\ell = +2)\rangle + e^{-i\theta}|J = -3, \sigma_-(\ell = -2)\rangle]$$

$$\psi(B_2) = \frac{1}{\sqrt{2}}[e^{i\theta}|J = 3, \sigma_+(\ell = +2)\rangle - e^{-i\theta}|J = -3, \sigma_-(\ell = -2)\rangle]. \tag{7}$$

Wave-functions associated to the E_1 doublet form conjugated partners with a total angular momentum $J = 1$ (E_1 is the irrep associated to modes presenting one quantum of angular momentum):

$$\psi_\pm(E_1) = |J = \pm 1, \sigma_\mp(\ell = \pm 2)\rangle. \tag{8}$$

Importantly, each 3-level fine structure presents the followings necessary assets for our lasing scheme: (1) only one state is entirely polarized σ_+ and only one is entirely polarized σ_-, so that these states present the highest gain when spin-polarizing the gain medium, and (2) these $\sigma_\pm$-polarized states present opposite OAM (i.e. $\pm\ell$). This is indeed the case for the states forming the E_1 and E_2 doublets. Although group theory does not allow identifying the spectral ordering of the states forming both fine structures, this ordering does not impact whatsoever the implementation of the lasing scheme.

Furthermore, finite elements numerical simulations have shown that symmetric and antisymmetric modes (i.e. A_1 and A_2 for $|\ell| = 1$, and B_1 and B_2 for $|\ell| = 2$) are maximally separated in energy (the doublets $E_{1,2}$ falling in-between); these simulations as well show that the highest energy state has A_2 (B_1) symmetry for the $|\ell| = 1$ ($|\ell| = 2$) manifold. The energy splitting, in both cases, is proportional to the hopping energy difference for photons polarized along and perpendicularly to the axis linking neighbouring pillars.

B. Extension to arbitrary n-pillar molecules

We now consider the general case of a n-pillar molecule whose symmetry elements form an ensemble corresponding to the C_{nv} group. Table II and III present the character table for arbitrary n, even and odd respectively.

Even number of pillars (n > 4)

For a molecule with an even number of pillars (but $n > 4$), the decomposition of the representation associated to the scalar wave-functions (i.e. without spin) is:

$$\Gamma_{\text{even}}^{(\text{scalar})} = A_1 \oplus B_1 \oplus E_1 \oplus E_2 \oplus E_3 \oplus ... \oplus E_{n/2-1}. \tag{9}$$

This indicates that the energy level structure is formed from 2 non-degenerate modes: A_1 ($\ell = 0$) and B_1 ($\ell = n/2$); and $n/2 - 1$ doublets associated to increasing $|\ell|$. A schematic representation of this level structure is presented in the left part of Fig. 8 (a).

To take into account the effect of spin-orbit coupling, we take the tensor product between the representations associated to the scalar wave-functions and E_1, corresponding to the spin moment. The decomposition of this tensor product gives:

$$E_1 \otimes \Gamma_{\text{even}}^{(\text{scalar})} = E_1 \otimes (A_1 \oplus B_1 \oplus E_1 \oplus E_2 \oplus E_3 \oplus ... \oplus E_{n/2-1})$$

$$= \underbrace{E_1}_{\ell=0} \oplus \underbrace{E_{n/2-1}}_{\ell=3} \oplus \underbrace{A_1 \oplus A_2 \oplus E_2}_{|\ell|=1} \oplus \underbrace{E_1 \oplus E_3}_{|\ell|=2} \oplus \underbrace{E_2 \oplus E_4}_{\ell=3} \oplus ... \oplus \underbrace{E_{n/2-3} \oplus E_{n/2-1}}_{|\ell|=4} \oplus \underbrace{B_1 \oplus B_2 \oplus E_{n/2-2}}_{|\ell|=n/2-1}.$$

$$\tag{10}$$

Modes	Functions	C_{nv} (n even)	E	$2C_n$	$2C_n^2$	$2C_n^3$	...	$C_n^{n/2}$	$3\sigma_v$	$3\sigma_d$
$|\ell| = 0$	z	A_1	1	1	1	1	...	1	1	1
		A_2	1	1	1	1	...	1	-1	-1
$|\ell| = n/2$		B_1	1	-1	1	-1	...	-1	1	-1
		B_2	1	-1	1	-1	...	-1	-1	1
$|\ell| = 1$	(x,y)	E_1	2	$2\cos(\alpha)$	$2\cos(2\alpha)$	$2\cos(3\alpha)$	...	$2\cos(\frac{n}{2}\alpha)$	0	0
$|\ell| = 2$		E_2	2	$2\cos(2\alpha)$	$2\cos(4\alpha)$	$2\cos(6\alpha)$	...	$2\cos(n\alpha)$	0	0
$\ell = 3$		E_3	2	$2\cos(3\alpha)$	$2\cos(6\alpha)$	$2\cos(9\alpha)$	...	$2\cos(\frac{3n}{2}\alpha)$	0	0
...	...	...	...	...	...	...	...	...	...	...
$|\ell| = n/2 - 1$		$E_{n/2-1}$	2	$2\cos((\frac{n}{2}-1)\alpha)$	$2\cos((n-2)\alpha)$	$2\cos((\frac{3n}{2}-3)\alpha)$	...	$2\cos(\frac{n}{2}(\frac{n}{2}-1)\alpha)$	0	0
		$\Gamma^{(\text{scalar})}$	n	0	0	0	...	0	2	0

TABLE II. General character table of a point group C_{nv} with n even. The bottom line corresponds to the characters of the reducible representation associated to the scalar wave-functions (i.e. without spin). ($\alpha = 2\pi/n$)

This decomposition (schematically presented in Fig. 8 (a)) shows that the $\ell = 0$ and $\ell = n/2$ manifolds, as in benzene, form degenerate doublets transforming as E_1 and $E_{n/2-1}$, respectively. Importantly, the $|\ell| = 1$ and $|\ell| = n/2-1$ manifolds split respectively in 3-level fine structures similar to the $|\ell| = 1$ and $|\ell| = 2$ manifolds of benzene. Therefore, both manifolds (indicated in red in Fig. 8 (a)) offer an appropriate fine structure for implementing our OAM lasing scheme.

The other manifolds of the eigenspectrum ($2 \leq |\ell| \leq n/2 - 2$) split in pairs of doublets transforming as $E_{|\ell|-1}$ and $E_{|\ell|+1}$. The associated wave-functions (with corresponding OAM) can be written as:

$$\psi_\pm(E_{|\ell|-1}) = |J = \pm(|\ell| + 1), \sigma_\mp\rangle \rightarrow \text{OAM} = \pm|\ell|$$
$$\psi_\pm(E_{|\ell|+1}) = |J = \pm(|\ell| - 1), \sigma_\pm\rangle \rightarrow \text{OAM} = \pm|\ell|. \tag{11}$$

Consequently, none of these manifolds offer an appropriate fine structure to implement our lasing scheme. Indeed, although all the states are circularly polarized, the polarization ($\sigma_\pm$) is not linked to a single chirality, thus preventing triggering lasing in a mode carrying a net OAM when spin-polarizing the gain medium.

4-pillar molecules

For a 4-pillar molecule, the decomposition described in Eq. (9) breaks down. In such a structure, $\ell = \pm 1$ modes transform according to the E_1 irrep of C_{2v}. Taking into account spin-orbit coupling, these states splits according to the decomposition:

$$E_1 \otimes E_1 = A_1 \oplus A_2 \oplus B_1 \oplus B_2, \tag{12}$$

thus forming 4 linearly polarized states carrying no net OAM. A possible way to understand this result in our particular system is that the symmetry of the square architecture does not lead to a mixing of the linear polarization when photons jump from one pillar to another.

Odd number of pillars

For a molecule presenting an odd number of pillars, the representation associated to scalar wave-functions is decomposed in irreps as:

$$\Gamma_{\text{odd}}^{(\text{scalar})} = A_1 \oplus E_1 \oplus E_2 \oplus E_3 \oplus ... \oplus E_{(n-1)/2}. \tag{13}$$

The main difference with the case of even molecules is the disappearance of the B_1 states, as an antisymmetric state (i.e. presenting a π phase shift between neighbouring pillars) is impossible in an odd number of pillars. A schematic representation of this level structure is presented in the left part of Fig. 8 (b).

When including the spin degree of freedom, the eigenspectrum (schematically depicted in the right part of Fig. 8 (b)) can be decomposed as:

Modes	Functions	C_{nv} (n odd)	E	$2C_n$	$2C_n^2$	$2C_n^3$	...	$2C_n^{\frac{n-1}{2}}$	$3\sigma_v$	$3\sigma_d$
$|\ell| = 0$	z	A_1	1	1	1	1	...	1	1	1
		A_2	1	1	1	1	...	1	-1	-1
$|\ell| = 1$	(x,y)	E_1	2	$2\cos(\alpha)$	$2\cos(2\alpha)$	$2\cos(3\alpha)$	...	$2\cos(\frac{n-1}{2}\alpha)$	0	0
$|\ell| = 2$		E_2	2	$2\cos(2\alpha)$	$2\cos(4\alpha)$	$2\cos(6\alpha)$	...	$2\cos((n-1)\alpha)$	0	0
$\ell = 3$		E_3	2	$2\cos(3\alpha)$	$2\cos(6\alpha)$	$2\cos(9\alpha)$	...	$2\cos(\frac{3(n-1)}{2}\alpha)$	0	0
...	...	...	...	...	...	...	...	...	...	...
$|\ell| = (n-1)/2$		$E_{(n-1)/2}$	2	$2\cos((\frac{n-1}{2})\alpha)$	$2\cos((n-1)\alpha)$	$2\cos((\frac{3(n-1)}{2})\alpha)$	...	$2\cos((\frac{n-1}{2})^2\alpha)$	0	0
		$\Gamma^{\text{(scalar)}}$	n	0	0	0	...	0	2	0

TABLE III. General character table of a point group C_{nv} with n odd. The bottom line corresponds to the characters of the reducible representation associated to the scalar wave-functions (i.e. without spin). ($\alpha = 2\pi/n$)

$$
\begin{aligned}
E_1 \otimes \Gamma^{\text{(scalar)}}_{\text{odd}} &= E_1 \otimes (A_1 \oplus E_1 \oplus E_2 \oplus E_3 \oplus ... \oplus E_{(n-1)/2}) \\
&= \underbrace{E_1}_{\ell=0} \oplus \underbrace{A_1 \oplus A_2 \oplus E_2}_{|\ell|=1} \oplus \underbrace{E_1 \oplus E_3}_{|\ell|=2} \oplus \underbrace{E_2 \oplus E_4}_{\ell=3} \oplus ... \oplus \underbrace{E_{(n-3)/2} \oplus E_{(n-1)/2}}_{|\ell|=(n-1)/2}.
\end{aligned} \tag{13}
$$

Here, contrary to the case of an even number of pillars, only the $|\ell| = 1$ manifold exhibits the appropriate 3-level structure (indicated in red in Fig. 8 (b)); all the other manifolds split in pairs of doublets that does not allow implementing our lasing scheme.

General guidelines related to the symmetry of the device

As show the above group theory arguments relating the symmetry of the device to its fine structure, the lasing scheme developed in this work is very general and is not limited to hexagonal symmetries (C_{6v}). The general guideline for designing a structure is that it must exhibit both circular symmetry (in order for angular momentum to be a conserved quantity of the system) *and* mirror symemtry (in order for the system to lase as well in CW and CCW propagating modes); the confluence of these two symmetries corresponds to C_{nv} symmetry groups.

Furthermore, as shown in Fig. 8 (a) and (b), a structure presenting a C_{nv} (with $n > 4$) symmetry will present the appropriate fine structure for the $|\ell| = 1$ manifold and, for n even, for the $|\ell| = n/2 - 1$ manifold. The physical reason why only these two manifolds can present the appropriate fine structure is related to the fact that photon polarization can only take values of $\pm\hbar$; therefore, due to the combined requirement of angular momentum and energy conservation, spin-orbit coupling can only mix together states $\ell = \pm 1$ (and $\ell = \pm n/2 - 1$, considering the periodic nature of a structure with an even number of pillars).

---

* These authors contributed equally to this work.

[1] M. S. Dresselhaus, G. Dresselhaus, and A. A. Jorio, *Group theory : application to the physics of condensed matter* (Springer-Verlag, 2008) p. 582.
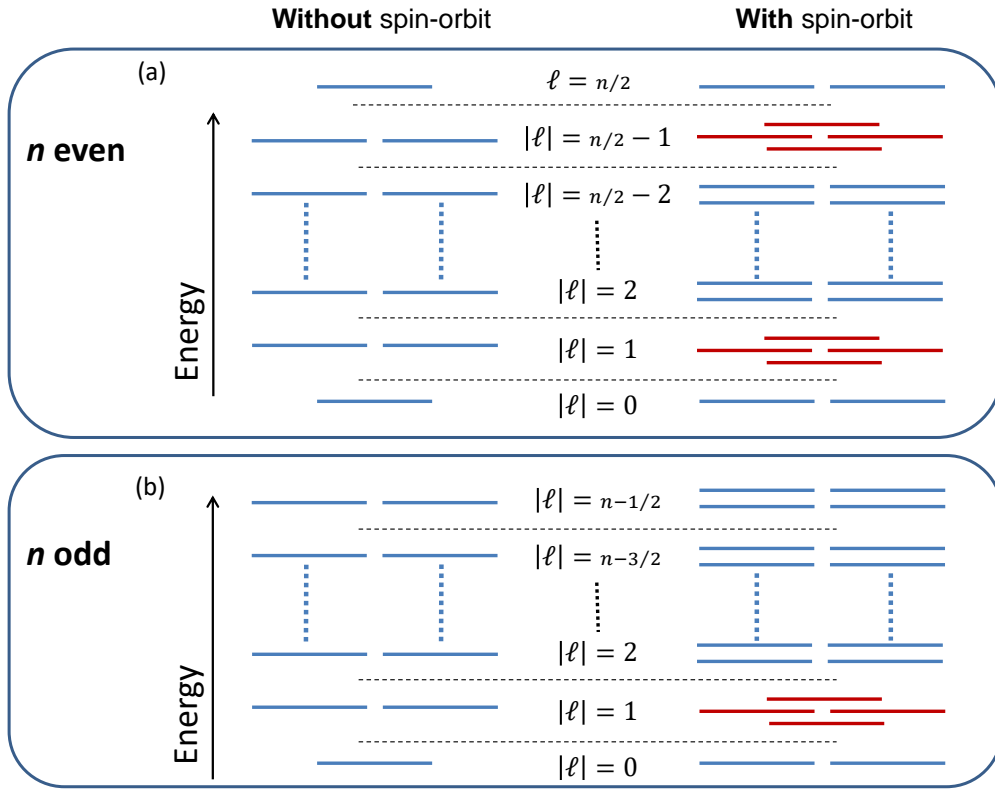
FIG. 8. Energy levels fine structure of a n-pillar photonic molecule for n even (top) and odd (bottom), with and without spin-orbit coupling. The 3-level fine structure necessary to implement our lasing scheme are presented in red.